

A Scalable Real-Time Architecture for Neural Oscillation Detection and Phase-Specific Stimulation

Christopher Thomas, *Member, IEEE*, and Thilo Womelsdorf

Abstract—Oscillations in the local field potential (LFP) of the brain are key signatures of neural information processing. Perturbing these oscillations at specific phases in order to alter neural information processing is an area of active research. Existing systems for phase-specific brain stimulation typically either do not offer real-time timing guarantees (desktop computer based systems) or require extensive programming of vendor-specific equipment. This work presents a real-time detection system architecture that is platform-agnostic and that scales to thousands of recording channels, validated using a proof-of-concept microcontroller-based implementation.

Index Terms—filtering, local field potential (LFP), neuroscience, time-frequency analysis

I. INTRODUCTION

Recording of electrical signals from neurons in human and animal brains is a well-established field [1]. Processing these signals reveals two related components: “spikes”, representing the firing of individual neurons near the pickup electrodes, and the “local field potential” (LFP), representing the aggregate activity of the larger population of neurons surrounding the electrode site [2]. Both of these signal components carry information: spikes via firing rate and timing [3] [4] [5] [6], and the LFP via the presence or absence of transient oscillations representing coherent activity of a large group of neurons [7] [8] [9] [10] [11]. The relative timing of spikes with respect to LFP oscillation phase has also been shown to encode information [12] [13] [6] [14] [15].

Artificial stimulation of human and animal brains (via electrical, optical, or other means) is also a field of active study [16] [17] [18] [19]. It has recently been shown that if LFP oscillations are present near a stimulation site, the timing of stimulation with respect to the LFP phase is important [20] [21] [22] [23]. In order to study this, it is necessary to perform “on-line” detection of transient LFP oscillations and to extract phase in real-time.

Existing experiments studying phase-specific stimulation can be divided into those that use a desktop computer to perform their signal processing [20] [24] [25] [21] and those which perform some or all of their signal processing on dedicated hardware [26] [27]. Both types of system have signal

processing latency that must be compensated for (typically 20-100 ms) [26] [21] but desktop computer based systems typically have substantial random variation (jitter) in processing and communications latency (typically 5-10 ms) [21], which is avoided in systems that keep the stimulation trigger processing entirely in dedicated hardware.

Low-latency signal processing systems running on dedicated hardware may be implemented in software running on dedicated digital signal processing (DSP) platforms [26] [28] or implemented using a field-programmable gate array (FPGA) tightly coupled to the recording system [27] [29]. Signal processing on dedicated hardware is widely used for processing of neural signals but is typically implemented ad-hoc.

The goal of this work is to present an open architecture for “on-line” LFP oscillation detection and for phase-aligned stimulation that is suitable for instantiation on conventional FPGA-based electrophysiology equipment and that is scalable to thousands of recording channels. The purpose of this architecture is to make experiment-specific FPGA-based closed-loop stimulation systems easier and faster to implement, as most of the implementation and debugging will already have been done.

II. BACKGROUND

A diagram of a typical electrophysiology recording and stimulation setup is shown in Figure 1. One or more probes, typically containing multiple electrical contacts per probe, are inserted into the brain. A “headstage” and a recording controller amplify and digitize the analog signals and forward them to a host computer. Electrical stimulation is performed using either a dedicated controller and probes or auxiliary functions of the controller, headstage, and probes used for recording. Recording and stimulation are typically performed while the subject performs some consistently-structured activity.

A typical single-channel recording waveform is shown in Figure 2 [30]. Noteworthy features are spikes (sub-millisecond duration) [31] [32], local field potential oscillations (typically 4-50 Hz and lasting for a small number of cycles [33]), and background noise (typically $\frac{1}{f^2}$ power-law noise at LFP frequencies [34] [35]). Spiking and LFP oscillation patterns vary widely depending on the region of the brain being measured [36] [37], and LFP oscillation duration (absolute and number of cycles) also depends strongly on the oscillation

C. Thomas and T. Womelsdorf are with the Department of Psychology, Vanderbilt University, Nashville, TN.

Manuscript received (date); revised (date).

This work has been submitted to the IEEE for possible publication. Copyright may be transferred without notice, after which this version may no longer be accessible.

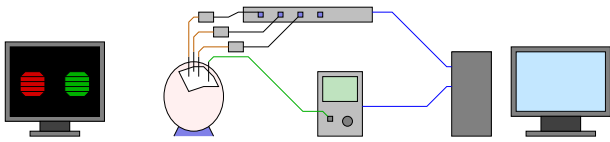


Fig. 1. Typical electrophysiology recording and stimulation setup using wire probes or linear silicon probes.

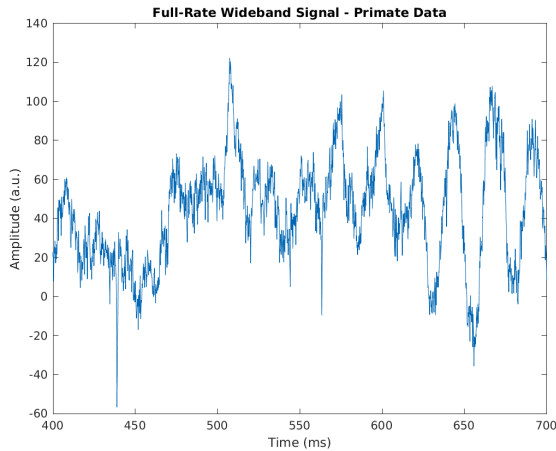


Fig. 2. Typical wide-band-signal recorded from a primate brain using tungsten wire probes [30]. Noteworthy features in this signal are sub-millisecond spikes and 20-25 Hz oscillations.

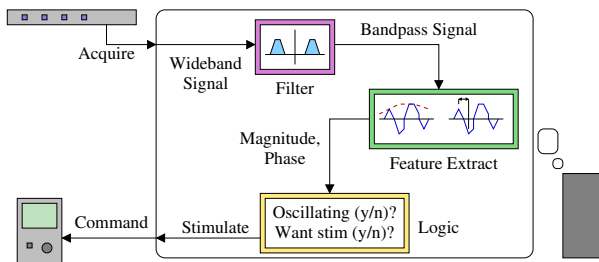


Fig. 3. Data processing flow within a typical electrophysiology recording and stimulation setup using a desktop computer for phase-aligned stimulation.

frequency [38]. At high frequencies (50-200 Hz), oscillations occur with durations of many cycles that are modulated by co-occurring low-frequency oscillations [10].

A typical closed-loop phase-aligned stimulation setup based on a desktop computer is shown in Figure 3. Signals are acquired using the recording controller and processed using “on-line” algorithms that are intended to function in real-time. When an oscillation occurs and stimulation is commanded during the experiment, the desktop computer waits until the appropriate oscillation phase before commanding the stimulation controller to activate.

Typical “on-line” oscillation detection and characterization algorithms are variants of a widely-used “offline” algorithm. In this offline algorithm, the LFP frequency band of interest is isolated and the analytic signal is computed, with the imaginary component provided by the Hilbert transform of

the band-pass-filtered signal. The analytic signal encodes the magnitude and phase of the original narrow-band signal [39] [25]. Oscillation events are identified by looking for magnitude excursions, with 2σ or 3σ from baseline magnitude being typical [20] [7] [26] [5]. Oscillation phase at any given instant is taken to be the analytic signal phase at the time of interest. For ease of reference, this will be referred to as the “offline Hilbert algorithm”.

For “on-line” implementation, band-pass filtering is typically performed using a finite impulse response filter (FIR) [26]. Magnitude and phase may be extracted via template-fitting [20] or interpolation between peaks, troughs, and zero-crossings in the narrow-band signal [39] [40]. Oscillation period may be estimated from the peaks, troughs, and zero-crossings or by using a filter bank with densely-spaced center frequencies and looking for the filter with the strongest response [26].

“Offline” algorithms for oscillation detection and parameterization are more varied [41], as they do not need to meet time constraints and they can consider both the past and future signal around a point of interest. Typical approaches that do not use the Hilbert transform involve decomposing the signal using either a fixed dictionary such as Gabor wavelets [42] or an optimized dictionary via sparse coding approaches [43] [44].

Hardware-based signal processing of electrophysiology signals typically involves electrophysiology controllers that expose digital signal processors (DSPs) or field-programmable gate arrays (FPGAs) to the user. These are programmable (DSP) or configurable (FPGA) hardware devices capable of running specialized computing operations much faster than general-purpose microprocessors. A typical electrophysiology controller that exposes DSP features to the user is the Tucker-Davis RZ2 BioAmp Processor [28] (based on the SHARC series of DSP processors). Typical electrophysiology controllers that expose FPGA features to the user are the Open Ephys acquisition board [45] [46] and the related Intan RHD recording controller [47] (both based on the Spartan 6 LX45 FPGA), and the NeuroLynx Hardware Processing Platform expansion board [29] (based on the Zynq 7045 SoC which integrates a Kintex 7 FPGA).

The performance metric that determines filtering and signal processing capability is the number of multiply-accumulate operations (MACs) that a given platform can perform per second. For DSP-based systems, the number of MACs is usually equivalent to the number of floating point operations per second (FLOPS). The SHARC DSP processors used by Tucker-Davis can perform 2.4 GFLOPS per core (at 400 MHz), for an aggregate maximum processing power of about 77 GMAC/sec (8 quad-core boards). For Xilinx-family FPGA-based systems, the number of MACs per second is determined by the number of “digital signal processing slices” and the rate at which these slices may be clocked. The XC6LX45 chip used in the Open Ephys and Intan controllers provides 5.8 GMAC/sec (58 units clocked at 100 MHz), some of which is used for the controller’s existing filtering operations. These controllers can acquire data from up to 1024 recording channels. The XC7Z045 chip used in the NeuroLynx

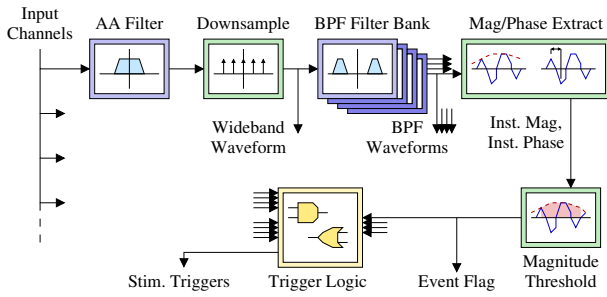


Fig. 4. Top-level oscillation detector architecture.

processing board provides 900 GMAC/sec (900 units clocked at 1 GHz), all of which is available for signal processing. The controller in which this board is installed can acquire data from up to 512 recording channels. While these examples are not exhaustive, it is reasonable to assume a processing budget of at least 2 MMAC/sec per channel, with up to 2 GMAC/sec per channel available in systems with more hardware resources available. LFP signal processing is typically performed at 1 ksp/s, with signals acquired at 25 ksp/s–40 ksp/s [26].

The desired goal is to detect local field potential oscillations while they are still happening (within 1–2 oscillation periods), and to accurately determine the oscillation phase so that phase-specific stimulation may be performed. The accuracy needed can be inferred from the number of phase bins used for spike-phase coding analyses; 4–10 phase bins are typical, with diminishing returns past 6 bins [5] [3]. This indicates that the full-width half-maximum of the phase error distribution should be 60 degrees or less.

III. IMPLEMENTATION

A block diagram of the oscillation detection architecture is shown in Figure 4. Full-rate data is passed through an anti-aliasing filter and downsampled. Downsampled data is passed through a filter bank that performs band-pass filtering, and an approximation of its instantaneous magnitude and phase is extracted. Event detection in each band is performed by magnitude thresholding, with inter-band logic building event triggers. A time shift is applied to correct the instantaneous phase estimate for filter delay, and trigger signals are generated using a target phase or a target time since zero-crossing. The output of the signal processing block is a set of narrow-band signal waveforms, estimates of instantaneous magnitude and phase associated with these waveforms, and event trigger logic signals suitable for driving neural stimulation equipment. Any of these outputs may be exposed to the host system.

The individual signal processing blocks in this architecture were implemented as modules, with the intention being that application-specific signal processing architectures would be built by assembling modules with a minimum of new code needed. Each of the modules was implemented in C++ and in Matlab, with FPGA-based implementations in development. The intention is to allow rapid prototyping via Matlab, embedded software implementations via C++, and full-scale hardware implementations via hardware description languages,

with confidence that all three types of implementation would produce comparable output if given the same input. As FPGA implementation is the end-goal, the modules are written to operate in a pipelined manner on a sample-by-sample basis (to facilitate translation to hardware).

Three closed-loop systems were assembled as reference implementations: One Matlab-based, one C++-based running on a desktop workstation, and one embedded C++ implementation running on a proof-of-concept “Burst Box” prototype. The Matlab implementation was used to verify that the architecture is conceptually sound; it was not otherwise resource-constrained (no memory or processing time limits, double-precision arithmetic). The workstation-based C++ implementation was used to verify that the architecture’s integer-arithmetic implementation produced output acceptably close to that of the Matlab implementation. While the workstation-based implementation was not explicitly memory-constrained, care was taken to keep internal structure sizes small enough to be instantiated on FPGAs. The embedded “Burst Box” prototype was used to verify that the architecture was capable of performing closed-loop stimulation in real-time with limited memory and a limited amount of processing power available.

Module library code and the reference implementations were made freely available under an open-source license [48].

A. Embedded Microcontroller Implementation

A block diagram of the embedded microcontroller-based implementation of the oscillation detector architecture is shown in Figure 5. Processing is restricted to one channel and one frequency band. Anti-aliasing and band-pass filters are implemented as infinite impulse response filters (IIR filters), to minimize processing load. Input signals may optionally be sampled at the downsampled rate directly without software anti-aliasing, reducing processing load but increasing signal noise due to aliasing artifacts. Approximate instantaneous magnitude and phase were extracted using peak, trough, and zero-crossing detection. Calculations were performed using 32-bit integer arithmetic with a signal range of 14 bits (to ensure sufficient head-room during multiply-accumulate operations). IIR filters were implemented as cascaded biquads with Direct Form I implementation. The a_0 biquad denominator coefficient was required to be a power of two, so that the $\frac{1}{a_0}$ operation could be performed as a bit-shift.

A block diagram of the firmware for the embedded implementation of the oscillation detector architecture is shown in Figure 6. Three concurrent execution threads are running: an interrupt service thread, which handles events that must occur with every real-time clock tick and complete within that timeslice; a high-priority polling thread, which is woken up by the real-time clock (preempting low-priority polling) but which may take multiple timeslices to complete; and a low-priority polling thread, which handles operations which do not require timing guarantees.

The physical implementation of the microcontroller-based prototype is shown in Figure 7 (the “Burst Box”). The microcontroller used is an Atmel ATmega2560 (8-bit, running at 16 MHz, with 8 kiB of SRAM); DSP performance was

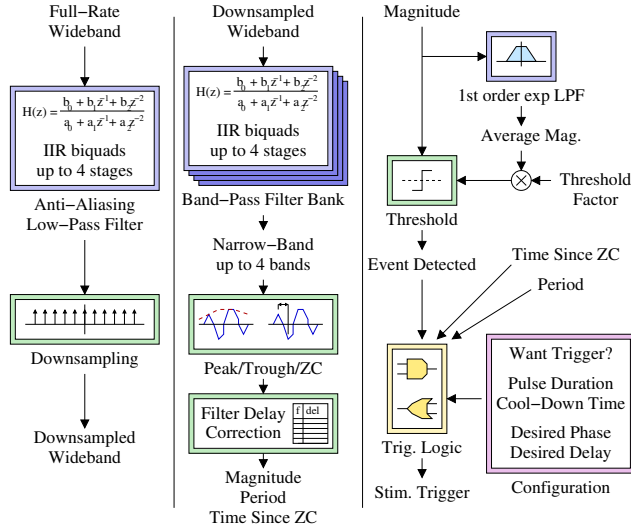


Fig. 5. Microcontroller-based implementation of the oscillation detector architecture.

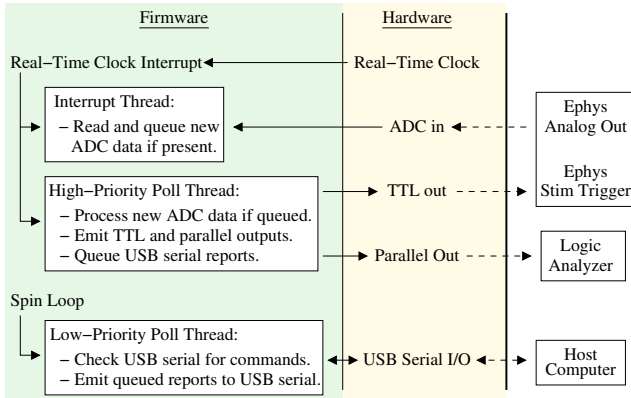


Fig. 6. Embedded oscillation detector firmware architecture.

benchmarked at approximately 100 kMAC/sec with 32-bit operands. “Full-rate” signals are sampled at 2.5 ksp/s using an external analog to digital converter and an analog anti-aliasing filter, and then downsampled to 500 sp/s internally (the “DSP rate”) after the application of a digital anti-aliasing filter. At 200 MAC/sample, this represents a worst-case lower bound to the processing budget available in real implementations.

A diagram of the hardware implementation of the “Burst Box” is shown in Figure 8. There is hardware support for up to 4 input channels, which constrains the processing budget further but allows testing of coincidence detection. The analog anti-aliasing filter in this prototype was implemented as an RC ladder filter for simplicity and to avoid any possibility of resonance from inductive components, with the tradeoff of having poor roll-off compared to a Butterworth implementation. For debugging purposes, the system can be configured to bypass the external analog-to-digital converter and use the microcontroller’s internal analog-to-digital converter at 500 sp/s without anti-aliasing.

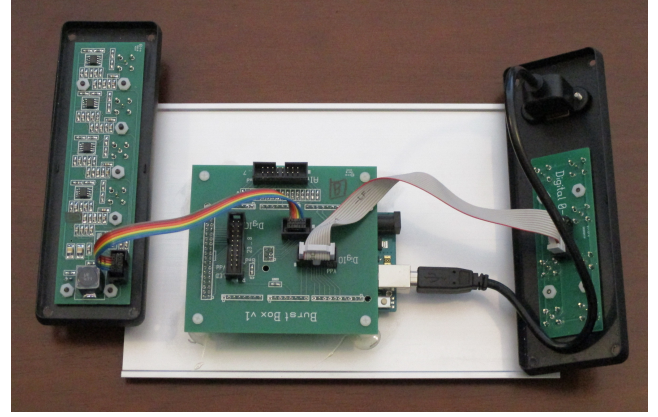


Fig. 7. Physical implementation of the microcontroller-based oscillation detector (“Burst Box”).

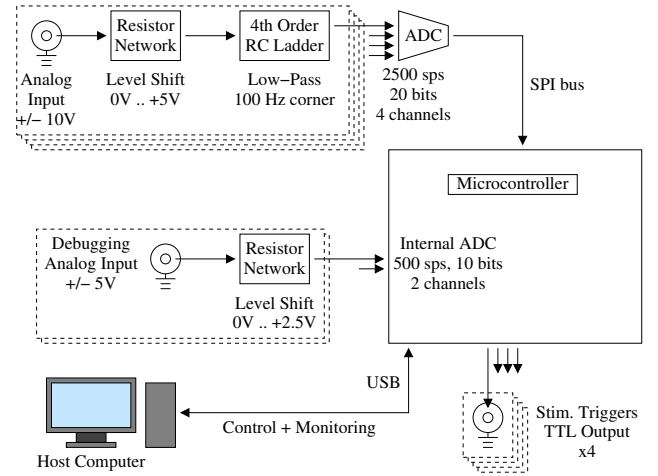


Fig. 8. Block diagram of the “Burst Box” hardware implementation.

TABLE I
SYNTHETIC DATASET NOISE BANDS

Freq (Hz) Band	4–7 theta	7–12 alpha	12–21 beta	21–36 gamma	36–63 gamma	63–108 gamma

IV. VALIDATION

A. Datasets

Two datasets were used for testing and validation of oscillation detector implementations. The first (the “synthetic” dataset) consisted of 5 minutes of $\frac{1}{f^2}$ noise (“red noise”) with tones overlaid. Tones had weak frequency chirping and amplitude ramping (less than 5% and 10% respectively), with cosine roll-off (Tukey window roll-off), and durations of 3–5 periods between midpoints of the roll-off flanks. Tones had a signal-to-noise ratio of 20 dB with respect to in-band noise; frequency bands used for noise calculations are shown in Table I. The “red noise” spectrum spanned from 2–200 Hz, with power concentrated at lower frequencies, so per-band adjustment of tone amplitude was necessary in order to have consistent signal-to-noise ratios.

The second dataset (“biological” dataset) consisted of a concatenated selection of recordings from a primate dataset

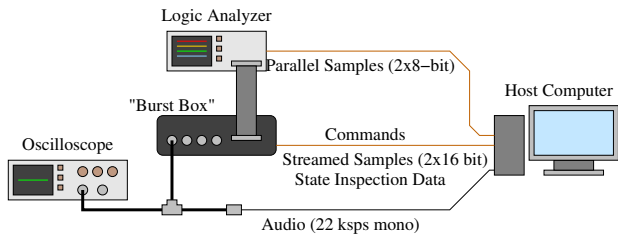


Fig. 9. Physical setup for validation tests.

[49]. The raw dataset consisted of “epochs” that were typically less than 10 seconds long, taken during individual task trials within one extended recording session. Signals from individual epochs were trimmed to time periods within the task that showed consistent activity with few electrical artifacts. Signals were evaluated on an epoch-by-epoch basis to reject records that contained artifacts within the trimming interval (typically large step transients caused by physical contact with equipment or 60 Hz tones coupled from nearby equipment). Remaining “clean” epochs were normalized to have consistent average power and were concatenated with an overlap of 0.5 s with linear interpolation between signals within the overlap interval. The intention was to produce an artifact-free signal of several minutes’ duration with biologically valid noise and oscillation features.

B. Test Procedure

Testing of the Matlab-based and workstation-based oscillation detectors was straightforward; both provide time series waveforms for all desired signals in their processing pipelines, with a common time reference between all signals. The challenge was to extract comparable information from the embedded microcontroller-based implementation during real-time tests.

The physical setup for real-time testing is shown in Figure 9. Signal waveforms were converted to sound files and played back to the “Burst Box” prototype via computer audio output. Volume settings for playback were adjusted until the output amplitude was approximately 3 V peak-to-peak, as measured using an oscilloscope. The “Burst Box” is capable of providing monitoring streams of two signals (typically one band-pass filtered waveform and one other signal derived from it). Tests with a given input waveform were run repeatedly, capturing different output waveform pairs, and these output waveform pairs were time-aligned using the band-pass filtered waveform as a reference (which should remain consistent between successive trials).

Signals streamed from the “Burst Box” could be read via two methods: parallel output via a logic header (8 bits per sample, precise timing and no dropped samples), and diagnostic output via the USB serial command interface (16 bits per sample, some dropped samples). Both capture methods were used. Unless otherwise indicated, the logic header output was used to generate plots.

Functionality exists for inspecting and modifying the internal state of the “Burst Box” using the serial command interface

TABLE II
INFINITE IMPULSE RESPONSE FILTER CONFIGURATIONS

Label	Type	Biquad Stages	Corners
anti-alias	low-pass	2	100 Hz
theta	band-pass	2	3 Hz-8 Hz
alpha	band-pass	2	6 Hz-16 Hz
beta	band-pass	2	12 Hz-32 Hz
low gamma	band-pass	2	24 Hz-64 Hz

for single-stepped testing. While this would provide all of the desired signals with high fidelity, it was not practical to use for full-duration test signals, due to being far slower than real-time testing.

C. Filtering

The purpose of filter validation is to confirm that the integer math C++ implementations of the oscillation detector’s filters match the behavior of the Matlab implementation of the same filters. This tested by plotting the inferred filter transfer functions measured during functionality tests against the ideal transfer functions.

Filter gain, phase shift, phase delay, and group delay were characterized by taking the Fourier transform of the time-aligned input and output waveforms for each filter under test. Dividing spectrum elements gives the frequency-domain transfer function directly, per Equation 1. This is smoothed, to reduce artifacts due to noise, and the phase is unwrapped. The phase delay and group delay are then computed per Equations 2 and 3, respectively. The derivative of $\phi(\omega)$ is approximated by taking the first difference and performing additional smoothing.

$$H(\omega) = \frac{\mathcal{F}\{y(t)\}}{\mathcal{F}\{x(t)\}} \quad (1)$$

$$G(\omega) = \|H(\omega)\|$$

$$\phi(\omega) = \arg(H(\omega))$$

$$\tau_\phi(\omega) = -\frac{\phi(\omega)}{\omega} \quad (2)$$

$$\tau_g(\omega) = -\frac{d\phi(\omega)}{d\omega} \quad (3)$$

The filter configurations used by the “Burst Box” prototype are shown in Table II. These were Butterworth infinite impulse response filters implemented as cascaded biquad stages. A representative plot of the designed and measured transfer functions for the “beta band” filter is shown in Figure 10, using the “synthetic” dataset as the input signal.

Within the regions of interest (blue in the single-filter plots, dark in the multi-filter plots), the designed and measured transfer functions are virtually identical. As a result, the filter implementation can be considered sound, and the Matlab models of the filters may be used as proxies for the real filter implementations without significant discrepancies expected.

All causal filters introduce delay into the filtered signal. For FIR filters, this delay is constant, and for IIR filters, different frequency components are delayed by different amounts. To

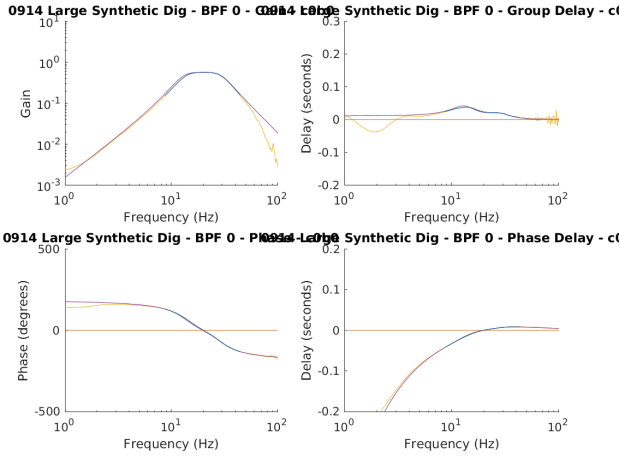


Fig. 10. Designed and measured transfer functions for the beta band filter.

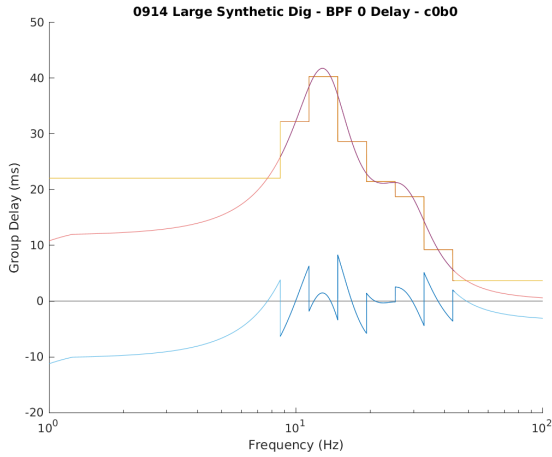


Fig. 11. Group delay calibration for the IIR beta band filter. The real group delay (red curve) is approximated by a lookup table of calibration delays (step-wise curve). The resulting delay error after calibration is shown in the blue curve.

allow later processing stages to compensate for this, a calibration table of delay vs frequency is built. Figure 11 shows an example of the calibrated delay (step-wise curve), actual delay (red curve), and delay error after calibration (blue curve) for the beta-band infinite impulse response filter shown in Figure 10.

D. Feature Extraction

Feature extraction was performed by looking for zero-crossings in the band-pass-filtered waveform, inferring period and phase from those zero crossings, and taking the maximum or minimum value of the waveform between successive zero-crossings as the magnitude of the signal. Feature extraction accuracy was characterized by comparing the oscillation detector's estimates of instantaneous magnitude, phase, and frequency to the instantaneous magnitude, phase, and frequency computed from the band-pass filtered signal by using Hilbert transform to derive the imaginary component of the analytic signal.

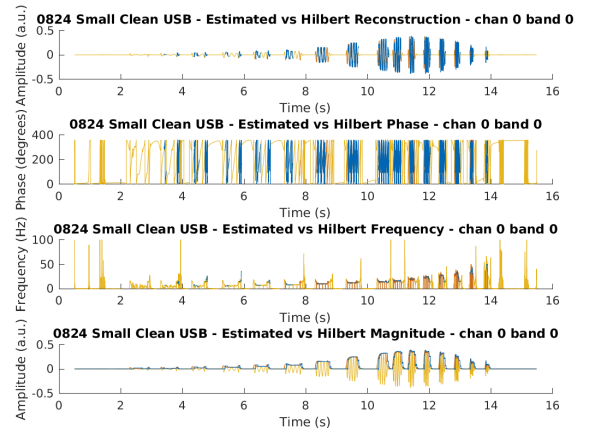


Fig. 12. Reconstructed vs analytic magnitude, phase, frequency, and waveform. Reconstruction was performed using peak, trough, and zero-crossing analysis of a short test waveform.

Figure 12 shows a representative reconstruction of magnitude, phase, frequency, and waveform using the peak-trough-ZC feature extractor (blue) and using the analytic signal (orange). Reconstruction was performed in regions where the magnitude was above-threshold, where threshold was set to twice the average magnitude. The analytic signal features are shown in yellow outside of these regions. This figure shows the analysis performed for a short test waveform, for illustration purposes.

“Delayed” and “zero-shift” versions of the band-pass filtered signal are considered. The “delayed” signal is the version received from the filter bank: frequencies are delayed by a fixed amount for FIR filters and a frequency-dependent amount for IIR filters (the “group delay” from Section IV-C). A “zero-shift” signal is computed by using the gain component $G(\omega)$ of the filter's transfer function (from Equation 1) as a non-causal filter to transform the wideband signal into a “zero-shift” band-pass signal (Equation 4). Time shift from the hardware anti-aliasing filter, software anti-aliasing filter, and software band-pass filters can be compensated in this manner.

$$\begin{aligned} Y_0(\omega) &= X(\omega) \cdot G(\omega) \\ y_0(t) &= \mathcal{F}^{-1}\{G(\omega) \cdot \mathcal{F}\{x(t)\}\} \end{aligned} \quad (4)$$

Comparison using the Hilbert transform of the original shifted signal $y(t)$ shows whether the oscillation detector's approximation of the Hilbert transform is accurate. Comparison using the Hilbert transform of the “zero-shift” signal $y_0(t)$ shows whether the oscillation detector's internal calibration of filter delay is accurate. Accurate estimation of instantaneous phase with respect to the wideband input signal is vital for phase-aligned neural stimulation.

Figure 13 shows histograms of magnitude error normalized to the analytic magnitude (relative error), and polar histograms of phase error with respect to analytic phase. The error distributions of the uncalibrated parameters with respect to the “delayed” waveform are shown in the top row and the error distributions of the calibrated parameters with respect to

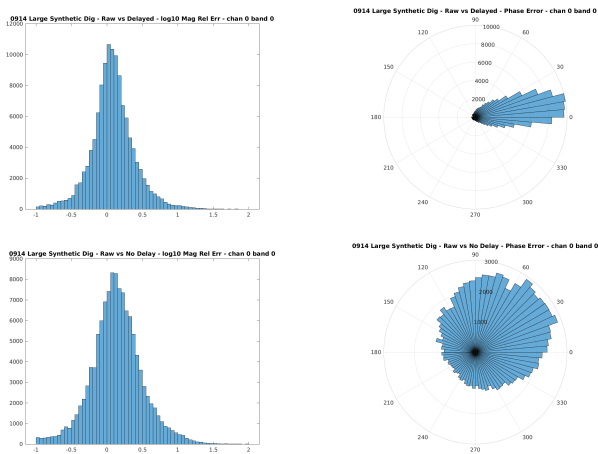


Fig. 13. Normalized reconstructed magnitude error (left) and absolute reconstructed phase error (right) with respect to analytic signal magnitude and phase for “delayed” (top) and “zero-shift” (bottom) band-pass filtered signals. Beta band IIR filter, “synthetic” dataset.

the “zero-shift” waveform are shown in the bottom row. This analysis was performed using the “synthetic” dataset.

Magnitude error distributions are broad in all cases. This is because the envelopes of event tones change on a timescale that is not substantially longer than the analysis timescale (one half-period of the event tone). As the magnitude estimate is out of date by half a period, there may be a considerable difference between the estimated and actual magnitudes. This can be seen in the bottom strip in Figure 12; the estimated envelope is time-shifted relative to the actual envelope.

Uncalibrated phase error with respect to the “delayed” wave is tightly clustered (35° FWHM, +10° offset). This represents the uncertainty in the phase estimate, caused by frequency shifts during the event, noise perturbing the detected locations of zero-crossings, and quantization of the detected half-period into an integer number of samples.

E. Phase-Aligned and Delay-Aligned Triggering

Trigger alignment was characterized by specifying a desired delay in milliseconds from the rising or falling zero-crossing, or a desired phase angle, and measuring the distribution of delays and phase angles at which stimulation trigger signals were actually generated. Histograms of the delay and phase error were generated with respect to the “delayed” band-pass signal without delay calibration and with respect to the “zero-shift” band-pass signal with delay calibration.

Figure 14 shows representative plots of trigger delay (left) and of delay error (right) for triggers scheduled with respect to the rising zero-crossing (top) or falling zero-crossing (bottom) of the input signal, with respect to the “delayed” signal, without calibration. These measurements were taken using the beta band IIR filter and the “synthetic” dataset. Under these test conditions, delay is tightly clustered (4 ms FWHM), but the error distribution has a broad base which grows to dominate the distribution for small delay values (less than 10 ms).

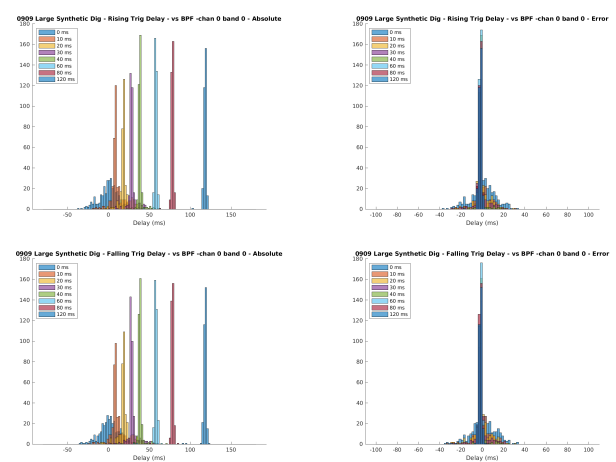


Fig. 14. Representative plots of trigger delay (left) and delay error (right) for triggers scheduled with respect to the rising zero-crossing (top) or falling zero-crossing (bottom) of the input signal. “Synthetic” dataset, beta band IIR filter, no calibration, “delayed” signal.

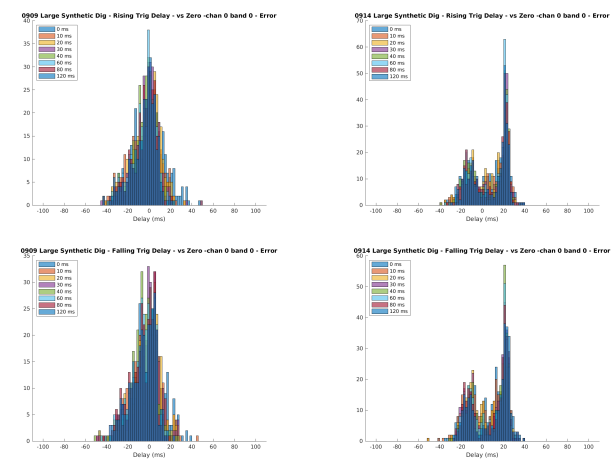


Fig. 15. Representative plots of trigger delay error without calibration (left) and with calibration (right) for triggers scheduled with respect to the rising zero-crossing (top) or falling zero-crossing (bottom) of the input signal. “Synthetic” dataset, beta band IIR filter, “zero-shift” signal.

Figure 15 shows representative plots of trigger delay error without calibration (left) and with calibration (right) for triggers scheduled with respect to the rising zero-crossing (top) or falling zero-crossing (bottom) of the input signal, with respect to the “zero-shift” signal. These measurements were taken using the beta band IIR filter and the “synthetic” dataset. Under these test conditions, calibration narrows the peak of the error distribution (to approx. 10 ms FWHM from approx. 20–30 ms FWHM), but a systematic delay of approx. 20 ms is applied, and a large secondary lobe at -20 ms results in mistimed triggers for a large fraction of cases.

Figure 16 shows representative plots of trigger phase (top) and trigger phase error statistics (bottom) for triggers scheduled with respect to specific phases of the input signal. Plots on the left show phase measured with respect to the peak and trough detector’s phase estimate, and plots on the right show phase measured with respect to the “delayed” signal, without calibration. These measurements were taken using the beta

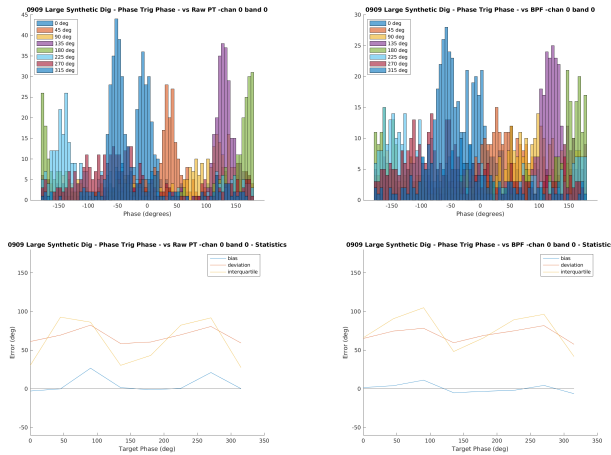


Fig. 16. Representative plots of trigger phase (top) and trigger phase error statistics (bottom) with respect to the peak and trough detector's phase estimate (left) and the phase of the analytic signal phase (right). "Synthetic" dataset, beta band IIR filter, "delayed" signal, no calibration.

band IIR filter and the "synthetic" dataset. Under these test conditions, phase with respect to the peak and trough phase estimate is clustered within the desired 60° FWHM for most target angles but shows scatter near 90° and 270° (phase targets near the zero-crossings). Phase with respect to the "delayed" band-pass filtered signal shows additional scatter, marginally meeting the 60° FWHM target.

V. CONCLUSION

A modular, scalable signal processing framework has been presented that is capable of detecting and characterizing oscillations on the local field potential of neural signals, and of generating trigger signals to allow phase-aligned and delay-aligned stimulation to be performed. As a case study, this framework was used to prototype a microcontroller-based oscillation detector that is capable of processing one signal channel and of responding to oscillation events within $\frac{3}{4}$ period of onset. The prototype's real-time estimate of signal phase has an error distribution FWHM of 35° with respect to the analytic signal. Triggers scheduled using a delay since a rising or falling zero-crossing have an error distribution FWHM of 4 ms, and triggers scheduled for a specific phase have an error distribution FWHM of approximately 60° with respect to the band-pass filtered signal, which meets the design requirements for a phase-aligned neural stimulation system. The framework was designed to be readily adapted to FPGA-based implementation for rapid development of closed-loop stimulation experiments using FPGA-based electrophysiology controllers.

REFERENCES

- [1] G. Buzsaki, N. Logothetis, and W. Singer, "Scaling brain size, keeping timing: Evolutionary preservation of brain rhythms," *Neuron*, vol. 80, no. 3, pp. 751–764, 2013.
- [2] G. Buzsaki, "Large-scale recording of neuronal ensembles," *Nature Neuroscience*, vol. 7, pp. 446–451, 2004.

- [3] T. Womelsdorf, B. Lima, M. Vinck, R. Oostenveld, W. Singer, S. Neun-schwander, and P. Fries, "Orientation selectivity and noise correlation in awake monkey area v1 are modulated by the gamma cycle," *Proceedings of the National Academy of Sciences*, vol. 109, no. 11, pp. 4302–4307, 2012.
- [4] C. Kayser, M. A. Montemurro, N. K. Logothetis, and S. Panzeri, "Spike-phase coding boosts and stabilizes information carried by spatial and temporal spike patterns," *Neuron*, vol. 61, no. 4, pp. 597–608, 2009.
- [5] B. Voloh, M. Oemisch, and T. Womelsdorf, "Phase of firing coding of learning variables across prefrontal cortex, anterior cingulate cortex and striatum during feature learning," *Nature Communications*, in press.
- [6] H. K. Turesson, N. K. Logothetis, and K. L. Hoffman, "Category-selective phase coding in the superior temporal sulcus," *Proceedings of the National Academy of Sciences*, vol. 109, no. 47, pp. 19438–19443, 2012.
- [7] M. Lundqvist, P. Herman, M. R. Warden, S. L. Brincat, and E. K. Miller, "Gamma and beta bursts during working memory readout suggest roles in its volitional control," *Nature Communications*, vol. 9, no. 394, 2018.
- [8] F. van Ede, A. J. Quinn, M. W. Wollrich, and A. C. Nobre, "Neural oscillations: Sustained rhythms or transient burst-events?" *Trends in Neurosciences*, vol. 41, no. 7, pp. 415–417, 2018.
- [9] M. A. Sherman, S. Lee, R. Shaw, S. Haegens, C. A. Thorn, M. S. Hamalainen, C. I. Moore, and S. R. Jones, "Neural mechanisms of transient neocortical beta rhythms: Converging evidence from humans, computational modeling, monkeys, and mice," *Proceedings of the National Academy of Sciences*, vol. 113, no. 33, pp. E4885–E4894, 2016.
- [10] B. Voloh, T. A. Valiante, S. Everling, and T. Womelsdorf, "Theta-gamma coordination between anterior cingulate and prefrontal cortex indexes correct attention shifts," *Proceedings of the National Academy of Sciences*, vol. 112, no. 27, pp. 8457–8462, 2015.
- [11] J. Feingold, D. J. Gibson, B. DePasquale, and A. M. Graybiel, "Bursts of beta oscillation differentiate postperformance activity in the striatum and motor cortex of monkeys performing movement tasks," *Proceedings of the National Academy of Sciences*, vol. 112, no. 44, pp. 12687–12692, 2015.
- [12] J. R. Huxter, T. J. Senior, K. Allen, and J. Csicsvari, "Theta phase-specific codes for two-dimensional position, trajectory and heading in the hippocampus," *Nature Neuroscience*, vol. 11, no. 5, pp. 587–594, May 2008.
- [13] M. Siegel, M. R. Warden, and E. K. Miller, "Phase-dependent neuronal coding of objects in short-term memory," *Proceedings of the National Academy of Sciences*, vol. 106, no. 50, pp. 21341–21346, 2009.
- [14] M. Vinck, T. Womelsdorf, and P. Fries, "Gamma-band synchronization and information transmission," in *Principles of Neural Coding*, R. Q. Quiroga and S. Panzeri, Eds. CRC Press, 2013, ch. 23, pp. 449–469.
- [15] M. Vinck, B. Lima, T. Womelsdorf, R. Oostenveld, W. Singer, S. Neun-schwander, and P. Fries, "Gamma-phase shifting in awake monkey visual cortex," *Journal of Neuroscience*, vol. 30, no. 4, pp. 1250–1257, 2010.
- [16] R. Polania, M. A. Nitsche, and C. C. Ruff, "Studying and modifying brain function with non-invasive brain stimulation," *Nature Neuroscience*, vol. 21, pp. 174–187, 2018.
- [17] M. A. Lebedev and M. A. L. Nicolelis, "Brain-machine interfaces: From basic science to neuroprostheses and neurorehabilitation," *Physiological Reviews*, vol. 97, pp. 767–837, 2017.
- [18] S. Qiao, J. I. Sedillo, K. A. Brown, B. Ferrentino, and B. Pesaran, "A causal network analysis of neuromodulation in the mood processing network," *Neuron*, vol. 107, pp. 1–14, 2020.
- [19] L. Grosenick, J. H. Marshel, and K. Deisseroth, "Closed-loop and activity-guided optogenetic control," *Neuron*, vol. 86, no. 1, pp. 106–139, 2015.
- [20] S. Zanos, I. Rembado, D. Chen, and E. E. Fetz, "Phase-locked stimulation during cortical beta oscillations produces bidirectional synaptic plasticity in awake monkeys," *Current Biology*, vol. 28, pp. 1–12, 2018.
- [21] J. H. Siegle and M. A. Wilson, "Enhancement of encoding and retrieval functions through theta phase-specific manipulation of hippocampus," p. e03061, 2014.
- [22] H. Cagnan, D. Pedrosa, S. Little, A. Pogosyan, B. Cheeran, T. Aziz, A. Green, J. Fitzgerald, T. Foltyniec, P. Limousin, L. Zrinzo, M. Hariz, K. J. Friston, T. Denison, and P. Brown, "Stimulating at the right time: phase-specific deep brain stimulation," *Brain*, vol. 140, no. 1, pp. 132–145, 2017.
- [23] G. Weerasinghe, B. Duchet, H. Cagnan, P. Brown, C. Bick, and R. Bogacz, "Predicting the effects of deep brain stimulation using a reduced coupled oscillator model," *PLOS Computational Biology*, vol. 15, no. 8, p. e1006575, 2019.
- [24] E. Blackwood, M. chen Lo, and A. S. Widge, "Continuous phase estimation for phase-locked neural stimulation using an autoregressive

- model for signal prediction,” in *Proc. 40th Conf. IEEE Engineering in Medicine and Biology Society*, 2018, pp. 4736–4739.
- [25] L. L. Chen, R. Madhaan, B. I. Rapoport, and W. S. Anderson, “Real-time brain oscillation detection and phase-locked stimulation using autoregressive spectral estimation and time-series forward prediction,” *IEEE Transactions on Biomedical Engineering*, vol. 60, no. 3, pp. 753–762, 2013.
- [26] G. Karvat, A. Schneider, M. Alyahyay, F. Steenbergen, M. Tangermann, and I. Diester, “Real-time detection of neural oscillation bursts allows behaviorally relevant neurofeedback,” *Communications Biology*, vol. 3, no. 72, pp. 1–10, 2020.
- [27] O. Talakoub, A. G. P. Schjetnan, T. A. Valiante, M. R. Popovic, and K. L. Hoffman, “Closed-loop interruption of hippocampal ripples through fornix stimulation in the non-human primate,” *Brain Stimulation*, vol. 9, pp. 911–918, 2016.
- [28] “RZ2 BioAmp Processor,” <https://www.tdt.com/files/manuals/Sys3Manual/RZ2.pdf>, accessed: 2020-08-26.
- [29] “Hardware Processing Platform (HPP): Getting Started Guide,” https://neuralynx.com/documents/HPP_Getting_Started_Guide.pdf, accessed: 2020-08-26.
- [30] M. Oemisch, S. Westendorff, M. Azimi, S. A. Hassani, S. Ardid, P. Tiesinga, and T. Womelsdorf, “Feature-specific prediction errors and surprise across macaque fronto-striatal circuits,” *Nature Communications*, vol. 10, no. 176, 2019.
- [31] B. P. Bean, “The action potential in mammalian central neurons,” *Nature Reviews Neuroscience*, vol. 8, pp. 451–465, 2007.
- [32] K. B. Boroujeni, P. Tiesinga, and T. Womelsdorf, “Adaptive spike-artifact removal from local field potentials uncovers prominent beta and gamma band neuronal synchronization,” *Journal of Neuroscience Methods*, p. 330:108485, 2020.
- [33] G. Buzsaki, C. A. Anastassiou, and C. Koch, “The origin of extracellular fields and currents – eeg, ecog, lfp and spikes,” *Nature Reviews Neuroscience*, vol. 13, pp. 407–420, May 2012.
- [34] K. J. Miller, L. B. Sorensen, J. G. Ojemann, and M. den Nijs, “Power-law scaling in the brain surface electric potential,” *PLOS Computational Biology*, vol. 5, no. 12, p. e1000609, 2009.
- [35] J. Milstein, F. Mormann, I. Fried, and C. Koch, “Neuronal shot noise and brownian $1/f^2$ behavior in the local field potential,” *PLOS One*, vol. 4, no. 2, p. e4338, 2009.
- [36] M. Steriade, “Corticothalamic resonance, states of vigilance and mentation,” *Neuroscience*, vol. 101, no. 2, pp. 243–276, 2000.
- [37] T. Womelsdorf, T. Valiante, N. T. Sahin, K. J. Miller, and P. Tiesinga, “Dynamic circuit motifs underlying rhythmic gain control, gating, and integration,” *Nature Neuroscience*, vol. 17, pp. 1031–1039, 2014.
- [38] G. Buzsaki, *Rhythms of the Brain*. Oxford University Press, 2006.
- [39] P. Y. Ktonas and N. Papp, “Instantaneous envelope and phase extraction from real signals: Theory, implementation, and an application to eeg analysis,” *Signal Processing*, vol. 2, no. 4, pp. 373–385, 1980.
- [40] S. Cole and B. Voytek, “Cycle-by-cycle analysis of neural oscillations,” *Journal of Neurophysiology*, vol. 122, no. 2, pp. 849–861, 2019.
- [41] J. C. Principe and A. J. Brockmeier, “Representing and decomposing neural potential signals,” *Current Opinion in Neurobiology*, vol. 31, pp. 13–17, 2015.
- [42] R. T. Canolty and T. Womelsdorf, “Multiscale adaptive gabor expansion (mage): Improved detection of transient oscillatory burst amplitude and phase,” 2019, <https://www.biorxiv.org/content/10.1101/369116v4.abstract>.
- [43] A. J. Brockmeier and J. C. Principe, “Learning recurrent waveforms within eegs,” *IEEE Transactions on Biomedical Engineering*, vol. 63, no. 1, pp. 43–54, 2016.
- [44] S. Hitziger, M. Clerc, S. Sallet, C. Bénar, and T. Papadopoulou, “Adaptive waveform learning: A framework for modeling variability in neurophysiological signals,” *IEEE Transactions on Signal Processing*, vol. 65, no. 16, pp. 4324–4338, 2017.
- [45] J. H. Siegle, A. C. Lopez, Y. A. Patel, K. Abramov, S. Ohayon, and J. Voigts, “Open ephys: an open-source plugin-based platform for multichannel electrophysiology,” *Journal of Neural Engineering*, vol. 14, no. 4, pp. 1–14, 2017.
- [46] “Acquisition board – Open Ephys,” <https://open-ephys.org/acq-board>, accessed: 2020-08-26.
- [47] “RHD USB/FPGA Interface: Rhythm USB3,” http://intantech.com/products_RHD2000_Rhythm_USB3.html, accessed: 2020-08-26.
- [48] “Attention Circuits Control Laboratory – NeuroLoop,” <https://github.com/att-circ-contrl/NeuroLoop>, accessed: 2020-09-14.
- [49] K. B. Boroujeni, M. Oemisch, S. alireza Hassani, and T. Womelsdorf, “Fast spiking interneuron activity in primate striatum tracks learning of

attention cues,” *Proceedings of the National Academy of Sciences*, vol. 117, no. 30, pp. 18 049–18 058, 2020.



Christopher Thomas Christopher Thomas is a research scientist with the Attention Circuits Control Laboratory in the Department of Psychology at Vanderbilt University, where he specializes in signal processing and embedded systems. He received his PhD from York University in Toronto, Canada for his work on image sensors.



brain activity dynamics relate to behavior.

Thilo Womelsdorf Thilo Womelsdorf is Associate Professor in the Departments of Psychology and Biomedical Engineering at Vanderbilt University, where he leads the Attention Circuits Control Laboratory. His research investigates how neural circuits learn and control attentional allocation in non-human primates and humans. Before arriving at Vanderbilt he led a systems neuroscience lab in Toronto (York University), receiving in 2017 the prestigious E.W.R. Steacie Memorial Fellowship for his work bridging the cell- and network- levels of understanding how